Fast Label-Free Cytoskeletal Network Imaging in Living Mammalian Cells

Pierre Bon,[†‡*] Sandrine Lécart,[§] Emmanuel Fort,[†] and Sandrine Lévêque-Fort[‡§]

[†]Institut Langevin, ESPCI ParisTech, Centre National de la Recherche Scientifique, Paris, France; [‡]Institut des Sciences Moléculaires d'Orsay (ISMO), Centre National de la Recherche Scientifique, Orsay, France; and [§]Centre de photonique Biomédicale, University Paris Sud, Orsay, France

ABSTRACT   We present a full-field technique that allows label-free cytoskeletal network imaging inside living cells. This noninvasive technique allows monitoring of the cytoskeleton dynamics as well as interactions between the latter and organelles on any timescale. It is based on high-resolution quantitative phase imaging (modified Quadriwave lateral shearing interferometry) and can be directly implemented using any optical microscope without modification. We demonstrate the capability of our setup on fixed and living Chinese hamster ovary cells, showing the cytoskeleton dynamics in lamellipodia during protrusion and mitochondria displacement along the cytoskeletal network. In addition, using the quantitative function of the technique, along with simulation tools, we determined the refractive index of a single tubulin microtubule to be $n_{tubu} = 2.36 \pm 0.6$ at $\lambda = 527$ nm.

The cytoskeleton is mainly composed of an actin and tubulin microtubule network, and it has many important roles at the cellular scale (1). It allows the cell to modify its shape, is implied in cell migration and adhesion processes, and is used as a support for organelle displacement inside cells.

Optical microscopy is useful for dynamic studies in which the cytoskeletal network is reorganizing quickly. However, due to the poor native interaction between light and this network fluorescence labeling is commonly used to image the cytoskeleton (2). Anisotropic approaches are also used on this kind of structure, as the cytoskeletal filaments may present refractive index anisotropy. Based on this property, polarized microscopy has been used to reveal the cytoskeleton (3). However, this technique is relatively slow compared to the cytoskeleton dynamics and requires perfectly stressless optics and a nondepolarizing sample. Differential interference contrast (DIC) approaches enhance the contrast in unstained cytoskeletal fibers (4) but also require precise light polarization control of both samples and optical components (for example, no plastic elements can be used for standard DIC). Moreover, the image has a gradient shape that induces loss of resolution and makes the images hard to interpret, especially in complex biological environments. Some DIC-based developments have been proposed that would make it possible to retrieve quantitative information from the sample and/or minimize the effects of depolarizing elements (5–8). Nonlinear interactions in second-harmonic generation (SHG) (9) that are sensitive to orientation and anisotropic refractive index are also applied to cytoskeleton imaging. Label-free imaging is thus obtained, but it requires a powerful laser and a scanning approach that may be too slow when fast dynamics need to be studied.

Although light interaction with a nonlabeled cytoskeleton is weak, with barely any absorption, there is a signature on the beam that travels through the structure even with nonpolarized illumination/detection. Indeed, as tubulin microtubules and actin filaments are denser than the cytoplasm, their respective refractive indices are also higher (10). This means that the light is slightly delayed by the cytoskeleton, leading to a possible contrast when looking at the phase component of light. In this article, we consider quantitative phase microscopy (QPM) based on quadriwave lateral shearing interferometry (QWLSI) (11). QWLSI makes it possible to image nonlabeled cells with a conventional transillumination microscope equipped with a halogen lamp. We propose a modified version of the QWLSI presented in our previous publication (11) that allows the fast, sensitive, and highly resolved imaging required to reveal cytoskeletal network dynamics in living cells. After discussing the signal/noise ratio (SNR) of our approach, we compare QPM with immunostaining of actin and tubulin microtubules on Chinese hamster ovary (CHO) cells, demonstrating the capability of QPM to visualize the cytoskeleton. Living wild-type (wt) CHO cells are then imaged at a high frame rate (2.5 Hz) to illustrate the spatiotemporal resolution of the technique for cytoskeleton imaging.

MATERIALS AND METHODS

Cell culture and immunofluorescence staining

CHO cells are grown in Dulbecco's modified Eagle's medium supplemented with 10% fetal bovine serum, 1% L-glutamin, and 1% penicillin/streptomycin (Life Technologies, Carlsbad, CA) in a cell-humidified culture incubator (37°C and 5% CO_2). After several days, cells are plated at low confluency on cleaned 25 mm type 1.5H glass coverslips (VWR, Radnor, PA).

For living cell observation, the cells are directly observed in their culture medium on the microscope.

To compare QPM and immunofluorescence imaging, a fixation and staining step is performed. Before fixation, all chemical reagents are prewarmed at 37°C. At 24 h after plating, cells are washed three times using PHEM buffer (60 mm PIPES, 25 mM HEPES, 5 mM EGTA, and 2 mM Mg acetate adjusted to pH 6.9 with 1 M KOH), preextracted for 1 min in 0.5% Triton

X-100 (Sigma-Aldrich, St. Louis, MO), and fixed for 20 min in 4% paraformaldehyde, 0.02% glutaraldehyde, and 0.5% Triton, then washed three times in phosphate-buffered saline (PBS) (Sigma-Aldrich). The samples are postfixed for 10 min with PBS with 0.1% Triton, reduced for 10 min with $NaBH_4$, and washed again in PBS. At this step, they are blocked for 15 min in PBS with 1% bovine serum albumin (BSA) before being incubated for 1 h at room temperature with 1:1000 mouse α-tubulin antibody (T6199, Sigma-Aldrich) in 0.1% BSA diluted in PBS, followed by three washes in PBS and incubation for 45 min with a 1:400 goat anti-mouse Alexa Fluor 488 (A-11029, Life Technologies) diluted in PBS with 0.1% BSA. Three additional washes are done in PBS. The second staining used a high-affinity F-actin probe, the Alexa Fluor 546 phalloidin (A-22283, Life Technologies). Cells were preincubated for 20 min in PBS with 1% BSA before addition of the phallotoxin staining solution for 20 min at room temperature. The samples were then washed in PBS and kept in PBS for direct microscope observation.

Imaging setup

To image the biological samples, we use a conventional nonmodified microscope (Ti, Nikon, Japan) equipped with an autofocus system (Perfect Focus System, Nikon, Japan) to ensure focus stability throughout the acquisition (≈ 20 min). For transmission QPM, the microscope is equipped with conventional halogen Köhler transillumination and a condenser of maximum numerical aperture $NA_{ill} = 0.52$. The illumination numerical aperture is set to the maximum to increase the QPM lateral resolution and to suppress diffraction artifacts around the structure (see next section). To limit photoxicity while keeping a good lateral resolution, a filter ($\lambda = 527 \pm 20$ nm) is inserted on the transillumination arm before the sample. (See Fig. 1 for a diagram of the imaging setup.)

For epiimmunofluorescence excitation, a fibered white-light source (IntensiLight, Nikon, Japan) is used. We choose two different filter sets to image sequentially Alexa 488 and Alexa 546. To avoid cross talk, the Alexa 488 cube is slightly blue-shifted (excitation, $\lambda = 460 \pm 10$ nm; emission, $\lambda = 527 \pm 12$ nm) and the Alexa 546 cube is red-shifted (excitation, $\lambda = 550 \pm 10$ nm; emission, $\lambda = 580 \pm 12$ nm).
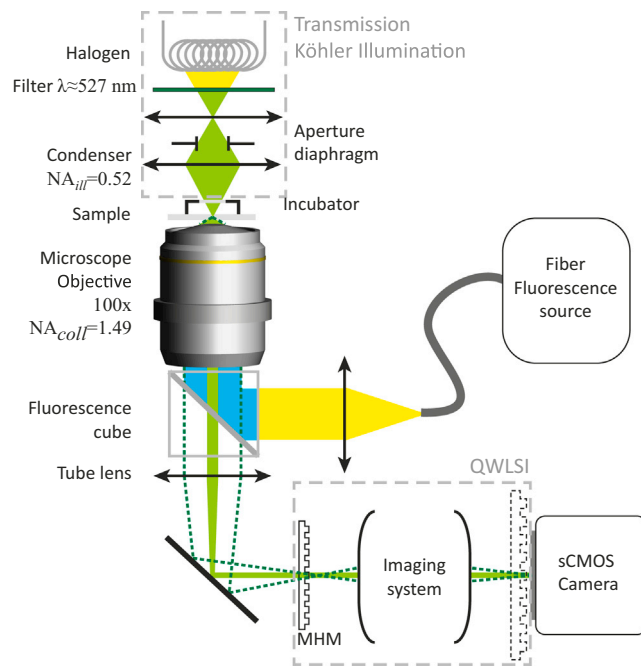

FIGURE 1   Schematic of the optical setup used in this article. To see this figure in color, go online.

For long-duration imaging, the microscope is equipped with an incubator (INU, Tokai HIT, Fujimiya City, Japan) to observe living samples at 37°C and 5% CO_2.

We image the samples with a $100\times$ $NA_{coll} = 1.49$ microscope objective (Nikon, Tokyo, Japan) on a modified commercial QWLSI (SID4-element, Phasics, Palaiseau, France). This QWLSI allows us to measure both the intensity and the optical path difference (OPD) of an image. The OPD is directly related to phase φ using the simple equation $\varphi = 2\pi \times OPD/\lambda$; for the rest of the discussion, the term phase image will be used to indicate this OPD image.

Both fluorescence and quantitative phase measurements are recorded with QWLSI, looking either at the intensity image during epifluorescence acquisitions or at phase during transilluminated acquisitions. This allows us to make direct overlay of images from fluorescence and phase acquisitions without numerical alignment.

Modified QWLSI for high-resolution and sensitive OPD determination

QWLSI is based on recording self-interference of the electromagnetic field in the microscope image plane. A QWLS interferogram allows direct measurement of both the intensity and OPD gradients of an image (11). To quantitatively retrieve the phase, the OPD gradients are numerically integrated with an algorithm suitable for any kind of sample (12). QWLSI has the significant advantage of furnishing achromatic measurements, thus enabling the use of polyachromatic illumination, such as the microscope halogen source.

We take advantage of the QWLSI capability of working with non-spatially-coherent illumination (11). This allows a better lateral resolution, r_{xy}^{φ}, and as the light is less coherent, the diffraction rings around the sample structures are reduced, leading to a less granular image aspect. These are key points in imaging the cytoskeleton—which is a very thin structure—within a dense cellular distribution.

The lateral resolution of a phase image is given by the Abbe resolution,

$$r_{xy}^{\varphi} = \frac{\lambda}{NA_{ill} + NA_{coll}} \approx 260 \text{ nm}. \quad (1)$$

In this article, we use a modified commercial QWLSI equipped with a Modified Hartmann Mask (MHM (13)) of sampling period $\Lambda = 10$ μm. This QWLSI perfectly samples the image; the Nyquist criterion is respected as $r_{xy}^{\varphi} \times M > 2 \times \Lambda$, with $M = 100$ for the microscope magnification.

To avoid any blurring effect due to the MHM (11), the grating-to-sensor distance is set to be as small as ≈ 100 μm. This is possible because the MHM is optically relayed in front of the camera sensor. It avoids any mechanical problem arising when the MHM is physically placed at such a small sensor distance.

A sCMOS camera (Neo, Andor, Belfast, Ireland) records the interferograms at a high frame rate of up to 100 frames/s in full-format image for a few seconds, but typically 50 frames/s for a user-defined duration. As we use a white-light incoherent halogen source, and as the QWLSI is self-referenced, the stability of the interferogram on the sensor allows direct averaging of the camera images without any fringe blurring effects. It enhances the SNR, as explained in the next section.

Spatiotemporal noise

The temporal and spatial noise of the QPM setup is studied here. The temporal noise is evaluated by acquiring a series of OPD images in a sample zone and considering each pixel stability. The spatial noise is evaluated by measuring the dispersion of OPD values on a sample with no cell. For both studies, the sample is a coverslip similar to those used for cell imaging (1.5 H type). The coveslip is covered with cell culture medium taken from a CHO culture to mimic the medium inhomogeneity during cell observations.

The temporal-phase deviation (Fig. 2 *a*) measured without any interferogram average is evaluated to have a standard deviation of $\sigma_{N=1}^{t} = 0.59$ nm with a 10 ms exposure time. This temporal noise falls to $\sigma_{N=20}^{t} = 0.11$ nm when 20 interferograms are averaged before calculating the phase. It is interesting to note that $\sigma_{N=20}^{t} < \sqrt{20} \times \sigma_{N=1}^{t}$, which means that the noise is not purely Gaussian and that the medium inhomogeneity also contributes to this temporal noise.

The spatial-phase noise is studied in Fig. 2 *b* by varying the number of averaged interferograms before OPD gradient computation. This noise decreases as a function of the number of averaged interferograms and tends to a horizontal asymptote, which means that even with a very high number of averaged interferograms, the spatial noise will never tend to 0. The major origin of this asymptote is the intrinsic coverslip roughness. Indeed, using an atomic force microscope (Nanowizard III, JPK Instruments, Berlin, Germany) in tapping mode, we measured the surface roughness to be $\sigma_{AFM} = 0.735$ nm on a 20×20 μm^2 surface. To deduce from this mechanical roughness the OPD roughness, only one coverslip interface has to be considered, although the light is transmitted through the whole coverglass. Indeed, the other interface is immersed in microscope oil, which has the property to perfectly match the coverglass refractive index. Considering that the refractive index of the coverslip is $n_{CS} = 1.515$, and assuming for optical considerations that the cell culture medium is water ($n_w = 1.333$), one can deduce a coverslip OPD roughness of $\sigma_{CS}^{s} = \sigma_{AFM} \times (n_{CS} - n_w) = 0.134$ nm. This value is close to the noise limit of Fig. 2 *b*, demonstrating that the coverslip is the major limitation to the sensitivity of averaged QPM.

For the rest of this study, we use 20 averaged images: it ensures a temporal OPD deviation of $\sigma_{N=20}^{t} = 0.11$ nm and a spatial OPD deviation of
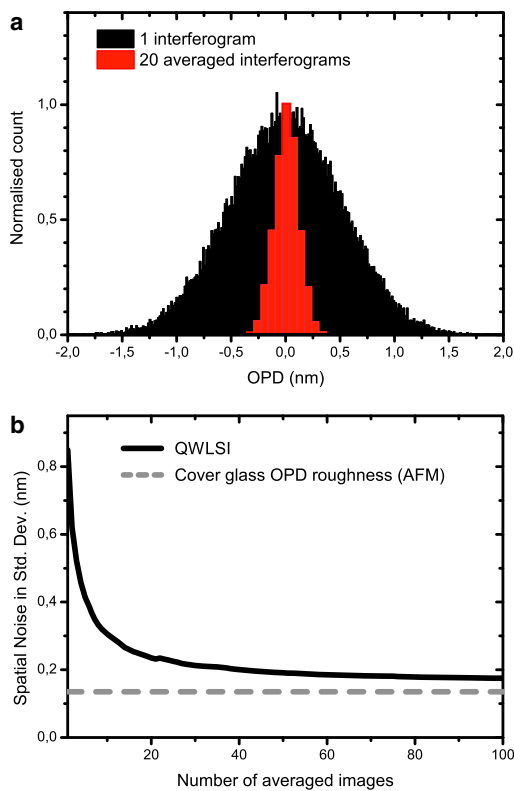

FIGURE 2 OPD noise of the setup measured in the sample immersion medium. (*a*) Temporal noise histogram: black, no interferogram average, $\sigma_{N=1}^{t} = 0.59$ nm; red, 20 averaged interferograms, $\sigma_{N=20}^{t} = 0.11$ nm. (*b*) Spatial noise: black line, standard deviation noise as a function of the number of averaged interferograms; gray dashed line, OPD noise deduced from the coverglass roughness measured with AFM. To see this figure in color, go online.

$\sigma_{N=20}^{s} = 0.23$ nm while keeping an OPD acquisition frame rate of 2.5 Hz. This sensitivity is enough to image a lipid bilayer with an SNR of 2 (11).

RESULTS

Multimodality immunofluorescence-QPM confirms label-free identification of cellular cytoskeletal fibers

To evaluate the capability of label-free cytoskeleton imaging, we consider correlative imaging between immunofluorescence (IF) and QPM on fixed CHO cells.

Raw QPM images have a strong total dynamic range (see, e.g., Fig. 3 *a*, where $\Delta OPD \approx 250$ nm) and it is hard to directly distinguish the poorly contrasted details within the cytoplasm. To enhance the cytoskeletal network, a numerical high-pass filtering is applied to the raw QPM image to suppress slowly varying phase information and thus reveal small structures (Fig. 3 *b*). Some filaments are visible on the high-pass QPM image with a good SNR, which is an indication of real progress in cytoskeleton imaging.

IF wide-field images of actin and tubulin filaments (Fig. 3, *c* and *d*, respectively) do not present cross talk and can be considered as highly specific to the labeled structure. From IF images and high-pass QPM images, composite images are computed (Fig. 3 *e*). The filament structures visible on QPM images are well colocalized with either tubulin microtubules or actin filaments, thus demonstrating that our technique can be used to visualize the cytoskeletal network without fluorescence. In the next section, we propose an approach to distinguish the tubulin from the actin filaments.

Quantitative analysis of phase values: a tool for differentiation between actin filaments and tubulin microtubules

QPM furnishes quantitative OPD values that can be interpreted as by the expression

$$OPD \approx \Delta n \times t, \qquad (2)$$

where Δn is the local difference in refractive index between the structure and its surrounding medium and t is the structure thickness. This formula neglects the diffraction effects and supposes that the illumination is a plane wave (i.e., $NA_{ill} = 0$). According to the literature, as the refractive index at $\lambda = 527$ nm of tubulin microtubules ($n_{tubu} = 2.8 \pm 0.1$ (14)) is strongly different from that of actin filaments ($n_{actin} = 1.57$ (15)), two fibers (one actin and one tubulin) with the same diameter can be theoretically differentiated one from the other considering only the OPD value. Unfortunately, because the cytoskeleton structures are not resolved, it is impossible to measure the diameter of each
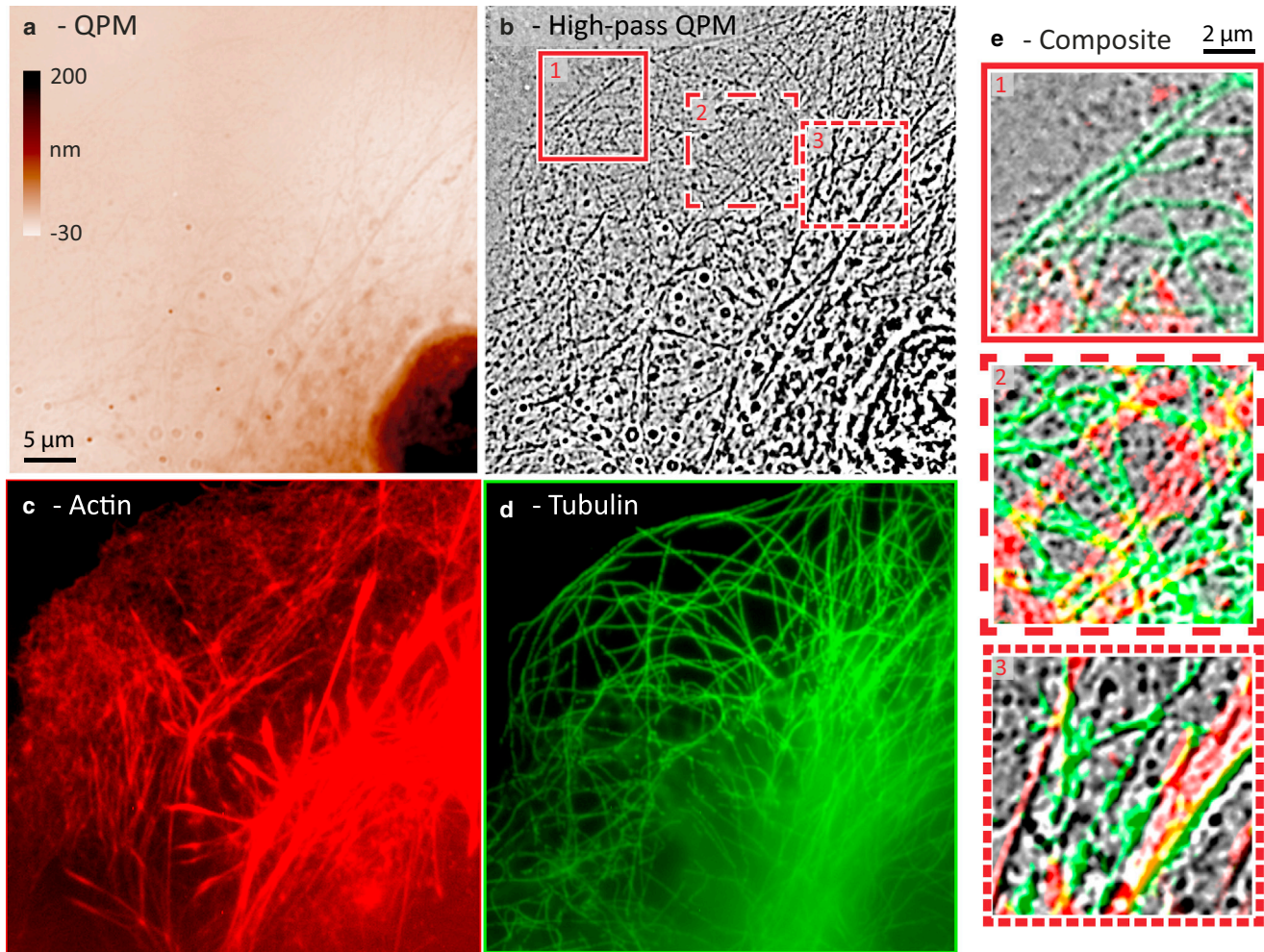
FIGURE 3   Fixed CHO cell. (*a*) QPM with the complete dynamic range observed in this cell. The nucleus is visible in the lower right corner. (*b*) Numerical high-pass filtering of the image in *a* to enhance the details in the phase image. Boxed areas numbered 1–3 are magnified in *e*. (*c*) Actin IF image using phalloidin-Alexa Fluor 546. (*d*) Tubulin IF image, using indirect staining with Alexa 488 labeling. (*e*) Composites of the images in *b–d*. A good spatial correlation between filament structures visible in high-pass QPM (*b*) and either actin (*c*) or tubulin (*d*) is visible in the composite images. To see this figure in color, go online.

fiber in the image, which prevents direct interpretation using this approach.

However, actin filaments and tubulin microtubules demonstrate different behavior: actin filaments, and especially the stress fibers visible with QPM, make bundles, whereas tubulin microtubules do not. This means that the dispersion of the OPD value is higher for actin filaments than for tubulin microtubules. Fig. 4 *a* sums up the cytoskeleton OPD values measured in fixed CHO cells with double IF labeling of actin and tubulin. The fiber OPD value is obtained by a Gaussian fit which is transverse to the fibers in raw OPD images. Statistics obtained for the two proteins show cumulative total lengths of 80 μm for tubulin microtubules and 225 μm for actin filaments.

As expected, the tubulin histogram is sharper than the actin histogram, with a maximum around $OPD_{tubu} = 1.58 \pm 0.4$ nm. The tubulin histogram can be fitted using two Gaussian curves, one centered at OPD_{tubu} and the other at $2 \times OPD_{tubu}$ (Fig. 4 *a*). One biological interpretation of this quantification is that only one or two tubulin microtubules are present at each measured spot.

Using this value of $OPD_{tubu} = 1.58$ nm, it is possible to determine the average refractive index of a tubulin microtubule. The model presented in equation 2 cannot be used directly, as the tubulin is not resolved and the illumination is far from a plane wave (i.e., $NA_{ill} = 0.52 \gg 0$). We thus consider simulation tools (16) to take into account the nonresolved shape of a microtubule (i.e., a cylinder of diameter 25 nm with a hole of diameter 14 nm) (Fig. 4 *b*) and illumination with $NA_{ill} \neq 0$. The OPD_{tubu} is obtained considering a refractive index of $n_{tubu} = 2.36 \pm 0.6$ (Fig. 4 *c*, *right*). Fig. 4 *d* shows a cross-section comparison between the simulated tubulin microtubule image and an experimental measurement.
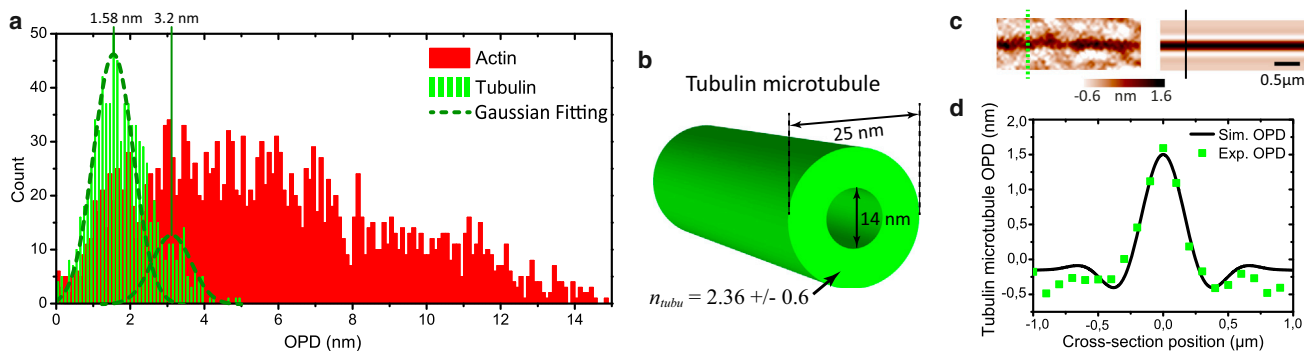
FIGURE 4 (*a*) OPD statistics of actin filaments (*red*) and tubulin microtubles (*green*), including a fit to the tubulin statistic using a double Gaussian approach (*dashed green line*). (*b*) The tubulin microtubule model used for simulation in *c* (*right*). (*c*) Experimental (*left*) and simulated (*right*) tubulin microtubule OPD. (*d*) Cross section of experimental (*green squares*) and simulated (*black line*) tubulin OPDs for the images in *c*. To see this figure in color, go online.

Label-free living-cell cytoskeleton QPM imaging

Let us consider the study of living wt CHO cells with QPM only. Fig. 5 shows the results of a 20 min experiment (see the Supporting Material).

As for fixed samples, the raw phase dynamic is large compared to the dynamic of the cytoskeleton (Fig. 5 *a*). High-pass filtering is applied to the raw phase (Fig. 5 *b*) to enhance the small details. The cytoskeletal network is visible, as are vesicles (dark spots) and mitochondria (dark dashes). Membrane dynamics, in particular ruffles and pro-trusions/retractions, are easily visible on high-pass-filtered QPM images.

It is thus possible to see the cytoskeleton growth during a protrusion (Fig. 5 *c*) and to monitor and track organelle movements on the network, such as those of a mitochon-drion (Fig. 5 *d*). OPDs introduced by cytoskeletal fibers have a typical value of 0.5 nm, and of up to 3.5 nm for the biggest fibers (actin stress fibers, for example); the majority of the fibers are thus detected with an SNR of >2.

Comparison between QPM and DIC imaging

DIC is an imaging technique that converts OPD information into intensity modulations (17). The obtained image carries the OPD gradient in one direction together with the sample absorption. Conventional DIC is qualitative by nature and requires polarization-free optical elements and samples. However, it is possible to obtain quantitative information with techniques derived from DIC (5–8), and some of these techniques overcome the problem of polarization (6,7).

For this study, we choose to compare conventional transmission DIC with our QWLSI-based technique. The
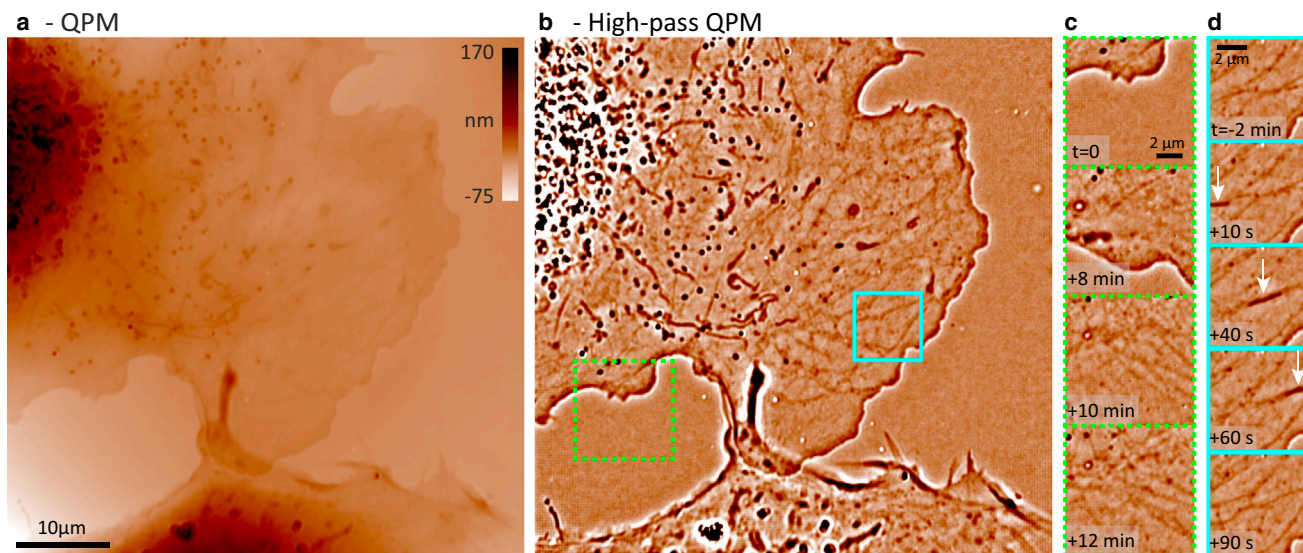

FIGURE 5 Living CHO cells observed for 20 min. (*a*) A single QPM image extracted from the series with the dynamics fixed to visualize all of the cell compounds. (*b*) Numerical high-pass filtering of the image in *a* to enhance the phase details. (*c* and *d*) Magnifications of the boxed areas in *b*. The protrusion in *b* (*green box*) was imaged for 12 min, and its membrane dynamics and cytoskeleton development are visible. Sequential images over 90 s of mitochondrion displacement on the cytoskeleton (*teal box, white arrows*). To see this figure in color, go online. Also, see Movie S1.

experimental comparison is made on an SP5 microscope (Leica Microsystems, Wetzlar, Germany) equipped with a $100\times$ objective of NA = 1.4. The transmission DIC is realized in a scanning mode at 50 Hz/line with a pixel sampling of 107 nm (approximately the same as the QPM image pixel size, i.e., 100 nm). This low scanning speed increases the DIC image SNR, and it takes ~10 s to make a 512×512 image with the same size as the QPM image. The observation wavelengths are $\lambda \approx 515$ nm for DIC and $\lambda \approx 527$ nm for QPM.

In Fig. 6, part of a living wt CHO cell is imaged with both DIC and QPM. The DIC image is recorded first and the QPM image ~15 s later (using manual switching). Some cytoskeleton structures that can be identified on the high-pass filtered QPM image (Fig. 6 c, lower) are barely visible on the DIC image (Fig. 6 c, upper). Cytoskeletal fibers are thus less contrasted with a commercial DIC than with our modified QWLSI-based QPM.

DISCUSSION

Label-free cytoskeleton imaging is possible using QPM based on a modified QWLSI setup. Raw camera image averaging allows enough sensitivity to visualize very small details such as cytoskeleton network and small-vesicle trafficking. The label-free approach is interesting, as it is not subject to photobleaching and thus the imaging process is noninvasive, quantitative, and fast. One of the key points used in this article is the capability of QWLSI to use non-spatially-coherent illumination. This ensures a better lateral resolution while decreasing the amplitude of diffraction artifacts commonly present in coherent imaging. During the last few years, several techniques have emerged that are based on quantitative phase imaging: Mach-Zender or Michelson designs (18–24), transport of intensity equations (25–27), phase engineering in the pupil (28,29), quantitative DIC (5,6), and the self-interference phenomenon (7,11,30,31). However, only a few of these techniques can work efficiently under non-spatially-coherent illumination (11,27,31), which is essential for cytoskeleton-like structures.

Indirect cytoskeleton imaging using intracellular bead movement monitoring by QPM has been developed recently (32), and we have demonstrated already that QPM with QWLSI reveals the biggest actin stress fibers (33), but the sensitivity at high resolution was not sufficient to contrast very small structures (such as tubulin). Here, we demonstrate that the modified QWLSI coupled with partially incoherent illumination leads to a much more sensitive approach.

Using correlative imaging between double IF on both actin (phalloidin labeled with Alexa 546) and tubulin (labeled using antibody-conjugated Alexa 488) and QPM, we found that the network structures visible in QPM are indeed cytoskeleton (both actin filaments and tubulin microtubules) and that our phase approach is sensitive enough to visualize most of the cytoskeleton using transmitted light only. However, very small actin filaments are barely visible on QPM images, indicating that monomers are not resolved with our technique.

By comparing our technique to the conventional DIC imaging approach, it can be seen that DIC is less sensitive than QPM with modified QWLSI. Most of the fibers that show good contrast with QPM are barely visible in DIC. Moreover, unlike QWLSI, DIC requires optics and samples that do not modify the light polarization and thus are not compatible with plastic elements (coverslip, heating chamber, etc.). DIC is essentially a contrast
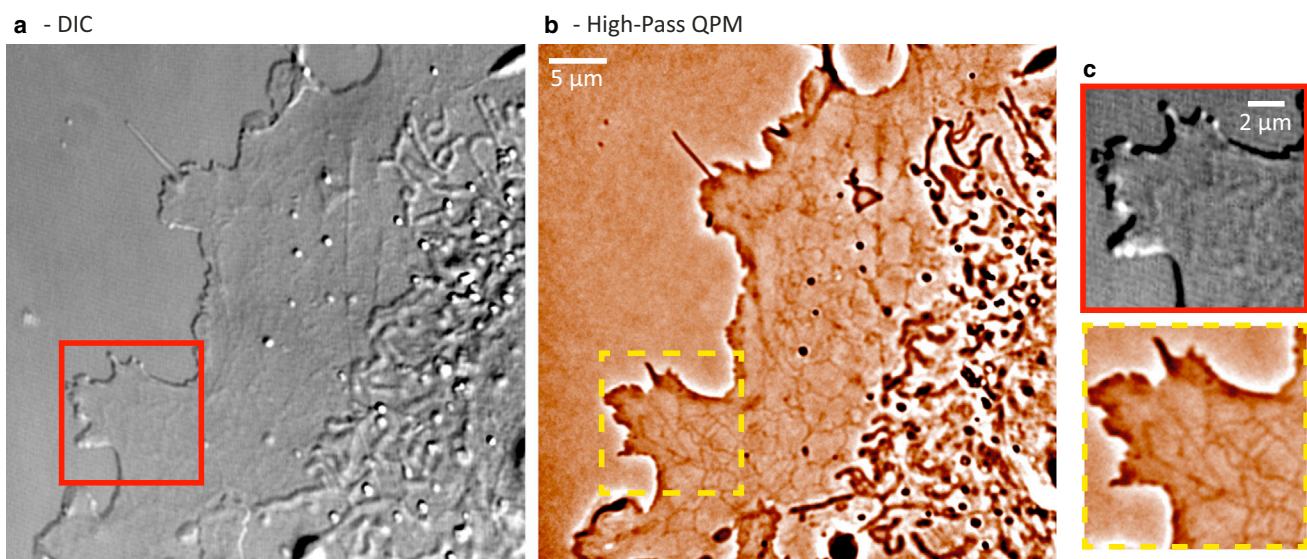

FIGURE 6 Living wt CHO cells observed at $100\times$ and NA 1.4. (a) DIC image. (b) High-pass filtered QPM (with QWLSI) image. (c) Zooms of boxed area in a (upper) and b (lower). To see this figure in color, go online.

technique, and quantitative studies such as refractive index quantification requires a setupmodification to be achieved.

Using the quantitative values measured with QPM, it is possible to statistically determine whether a single detected fiber is composed of actin or tubulin: at $\lambda = 527$ nm, tubulin fibers have an OPD of 1.58 ± 0.4 nm, whereas actin fibers can have any value from 0 to ~15 nm. QPM differentiation between actin and tubulin requires thin samples and is not as good as that obtained with double IF labeling. However, it can be applied to samples that are very sensitive to phototoxicity, such as neurons or stem cells, or for fast and/or long-duration imaging where photobleaching is a major limitation. Moreover, using this value of $OPD_{tubu} = 1.58 \pm 0.4$ nm and simulation tools (16), we determine the refractive index of tubulin microtubules to be $n_{tubu} = 2.36 \pm 0.6$, a value in agreement with those in the literature (14).

One of the advantages of QPM is its ability to image whole cell structures and not just the cytoskeleton. It facilitates our understanding of dynamic processes such as organelle movements or cell protrusions/retractions using only one imaging mode. The temporal resolution is 2.5 Hz in this study, and it is perfectly suitable to this kind of application. To increase the temporal resolution, a camera with a higher frame rate might be considered. The nonspecificity of our phase technique is also its major limitation: where the sample is particularly complex, with a 3D structure (around the nucleus or near the Golgi apparatus, for example), it is hard to distinguish the smallest cytoskeletal structures from their environment. However, in lamellipodia and, more generally, in thin cell parts, the cytoskeletal network and its interaction with organelles can easily be monitored with an SNR >2.

The simplicity of our white-light transmission technique and its ability to be plugged into any optical microscope setup allows for broad use of it in any experiment that requires the monitoring of cytoskeletal network or cell/organelle motility, as long as the sample is thin enough. For example, it would be useful in optogenetic experiments to visualize the recruitment of actin/tubulin when the sample is stimulated, or in combination with single-molecule imaging to follow the interaction of the protein cargo with the cytoskeletal network.

SUPPORTING MATERIAL

One movie is available at http://www.biophysj.org/biophysj/supplemental/S0006-3495(14)00229-X.

REFERENCES

1. Frixione, E. 2000. Recurring views on the structure and function of the cytoskeleton: a 300-year epic. *Cell Motil. Cytoskeleton.* 46:73–94.

2. Xu, K., H. P. Babcock, and X. Zhuang. 2012. Dual-objective STORM reveals three-dimensional filament organization in the actin cytoskeleton. *Nat. Methods.* 9:185–188.

3. Kuhn, J. R., Z. Wu, and M. Poenie. 2001. Modulated polarization microscopy: a promising new approach to visualizing cytoskeletal dynamics in living cells. *Biophys. J.* 80:972–985.

4. Allen, R. D., N. S. Allen, and J. L. Travis. 1981. Video-enhanced contrast, differential interference contrast (AVEC-DIC) microscopy: a new method capable of analyzing microtubule-related motility in the reticulopodial network of *Allogromia laticollaris. Cell Motil.* 1:291–302.

5. Arnison, M. R., K. G. Larkin, …, C. J. Cogswell. 2004. Linear phase imaging using differential interference contrast microscopy. *J. Microsc.* 214:7–12.

6. McIntyre, T. J., C. Maurer, …, M. Ritsch-Marte. 2010. Quantitative SLM-based differential interference contrast imaging. *Opt. Express.* 18:14063–14078.

7. Fu, D., S. Oh, …, M. S. Feld. 2010. Quantitative DIC microscopy using an off-axis self-interference approach. *Opt. Lett.* 35:2370–2372.

8. Duncan, D. D., D. G. Fischer, …, S. A. Prahl. 2011. Quantitative Carré differential interference contrast microscopy to assess phase and amplitude. *J. Opt. Soc. Am. A Opt. Image Sci. Vis.* 28:1297–1306.

9. Psilodimitrakopoulos, S., V. Petegnief, …, P. Loza-Alvarez. 2013. Quantitative imaging of microtubule alteration as an early marker of axonal degeneration after ischemia in neurons. *Biophys. J.* 104: 968–975.

10. Barer, R. 1952. Interference microscopy and mass determination. *Nature.* 169:366–367.

11. Bon, P., G. Maucort, …, S. Monneret. 2009. Quadriwave lateral shearing interferometry for quantitative phase microscopy of living cells. *Opt. Express.* 17:13080–13094.

12. Bon, P., S. Monneret, and B. Wattellier. 2012. Noniterative boundary-artifact-free wavefront reconstruction from its derivatives. *Appl. Opt.* 51:5698–5704.

13. Primot, J., and N. Guérineau. 2000. Extended hartmann test based on the pseudoguiding property of a hartmann mask completed by a phase chessboard. *Appl. Opt.* 39:5715–5720.

14. Mershin, A., A. A. Kolomenski, …, D. V. Nanopoulos. 2004. Tubulin dipole moment, dielectric constant and quantum behavior: computer simulations, experimental results and suggestions. *Biosystems.* 77: 73–85.

15. Andersen, M., and S. Nir. 1977. Van der Waals parameters, refractive indices and dispersion equations of spectrin, actin and other mammalian proteins. *Polymer.* 18:867–870.

16. Bon, P., B. Wattellier, and S. Monneret. 2012. Modeling quantitative phase image formation under tilted illuminations. *Opt. Lett.* 37: 1718–1720.

17. Nomarski, G. 1955. Nouveau dispositif pour l'observation en contraste de phase differentiel. *J. Phys. Radium.* 16:S88.

18. Cuche, E., P. Marquet, and C. Depeursinge. 1999. Simultaneous amplitude-contrast and quantitative phase-contrast microscopy by numerical reconstruction of Fresnel off-axis holograms. *Appl. Opt.* 38:6994–7001.

19. Popescu, G., L. P. Deflores, …, M. S. Feld. 2004. Fourier phase microscopy for investigation of biological structures and dynamics. *Opt. Lett.* 29:2503–2505.

20. Debailleul, M., V. Georges, …, O. Haeberlé. 2009. High-resolution three-dimensional tomographic diffractive microscopy of transparent inorganic and biological samples. *Opt. Lett.* 34:79–81.

21. Kemper, B., A. Vollmer, …, G. von Bally. 2011. Simplified approach for quantitative digital holographic phase contrast imaging of living cells. *J. Biomed. Opt.* 16:026014.

22. Choi, Y., T. D. Yang, …, W. Choi. 2011. Full-field and single-shot quantitative phase microscopy using dynamic speckle illumination. *Opt. Lett.* 36:2465–2467.

23. Shaked, N. T. 2012. Quantitative phase microscopy of biological samples using a portable interferometer. *Opt. Lett.* 37:2016–2018.

24. Bhaduri, B., K. Tangella, and G. Popescu. 2013. Fourier phase microscopy with white light. *Biomed. Opt. Express.* 4:1434–1441.

25. Barty, A., K. A. Nugent, …, A. Roberts. 1998. Quantitative optical phase microscopy. *Opt. Lett.* 23:817–819.

26. Kou, S. S., L. Waller, …, C. J. R. Sheppard. 2010. Transport-of-intensity approach to differential interference contrast (TI-DIC) microscopy for quantitative phase imaging. *Opt. Lett.* 35:447–449.

27. Phillips, K. G., S. L. Jacques, and O. J. T. McCarty. 2012. Measurement of single cell refractive index, dry mass, volume, and density using a transillumination microscope. *Phys. Rev. Lett.* 109:118105.

28. Bernet, S., A. Jesacher, …, M. Ritsch-Marte. 2006. Quantitative imaging of complex samples by spiral phase contrast microscopy. *Opt. Express.* 14:3792–3805.

29. Wang, Z., L. Millet, …, G. Popescu. 2011. Spatial light interference microscopy (SLIM). *Opt. Express.* 19:1016–1026.

30. Iglesias, I. 2011. Pyramid phase microscopy. *Opt. Lett.* 36:3636–3638.

31. Parthasarathy, A. B., K. K. Chu, …, J. Mertz. 2012. Quantitative phase imaging using a partitioned detection aperture. *Opt. Lett.* 37:4062–4064.

32. Barroso, Á., M. Woerdemann, …, C. Denz. 2012. Three-dimensional exploration and mechano-biophysical analysis of the inner structure of living cells. *Small.* 9:885–893.

33. Bon, P., J. Savatier, …, S. Monneret. 2012. Optical detection and measurement of living cell morphometric features with single-shot quantitative phase microscopy. *J. Biomed. Opt.* 17:076004.

Fast Label-Free Cytoskeletal Network Imaging in Living Mammalian Cells

Pierre Bon,[†‡]* Sandrine Lécart,[§] Emmanuel Fort,[†] and Sandrine Lévêque-Fort[‡§]

[†]Institut Langevin, ESPCI ParisTech, Centre National de la Recherche Scientifique, Paris, France; [‡]Institut des Sciences Moléculaires d'Orsay (ISMO), Centre National de la Recherche Scientifique, Orsay, France; and [§]Centre de photonique Biomédicale, University Paris Sud, Orsay, France

Movie:

Living CHO cells observed during 20 minutes. (left) QPM imaging. The dynamic is fixed to visualize the entire cell compounds. (right) Numerical high-pass filtering of (left) to enhance the details in the phase image.